A&A 565, A34 (2014)
DOI: 10.1051/0004-6361/201323129

Astronomy & Astrophysics

A subarcsecond study of the hot molecular core in G023.01−00.41⋆,⋆⋆

A. Sanna[1], R. Cesaroni[2], L. Moscadelli[2], Q. Zhang[3], K. M. Menten[1], S. Molinari[4], A. Caratti o Garatti[1], and J. M. De Buizer[5]

[1] Max-Planck-Institut für Radioastronomie, Auf dem Hügel 69, 53121 Bonn, Germany
e-mail: asanna@mpifr-bonn.mpg.de
[2] INAF, Osservatorio Astrofisico di Arcetri, Largo E. Fermi 5, 50125 Firenze, Italy
[3] Harvard-Smithsonian Center for Astrophysics, 60 Garden Street, Cambridge MA 02138, USA
[4] INAF-IFSI, via Fosso del Cavaliere 100, 00133 Roma, Italy
[5] Stratospheric Observatory for Infrared Astronomy-USRA, NASA Ames Research Center, MS.N232-12, Moffet Field CA 94035, USA

Received 25 November 2013 / Accepted 13 February 2014

ABSTRACT

Context. Searching for disk-outflow systems in massive star-forming regions is a key to assessing the main physical processes in the recipe of massive star formation.
Aims. We have selected a hot molecular core (HMC) in the high-mass star-forming region G023.01−00.41, where VLBI multi-epoch observations of water and methanol masers have suggested the existence of rotation and expansion within 2000 AU of its center. Our purpose is to image the thermal line and continuum emission at millimeter wavelengths to establish the physical parameters and velocity field of the gas in the region.
Methods. We performed SMA observations at 1.3 mm with both the most extended and compact array configurations, providing subarcsecond and high sensitivity maps of various molecular lines, including both hot-core and outflow tracers. We also reconstructed the spectral energy distribution of the region from millimeter to near infrared wavelengths, using the *Herschel*/Hi-GAL maps, as well as archival data.
Results. From the spectral energy distribution, we derive a bolometric luminosity of $\sim 4 \times 10^4$ $L_\odot$. Our interferometric observations reveal that the distribution of dense gas and dust in the HMC is significantly flattened and extends up to a radius of 8000 AU from the center of radio continuum and maser emission in the region. The equatorial plane of this HMC is strictly perpendicular to the elongation of the collimated bipolar outflow, as imaged on scales of ∼0.1–0.5 pc in the main CO isotopomers, as well as in the SiO(5–4) line. In the innermost HMC regions ($\lesssim$1000 AU), the velocity field traced by the CH_3CN (12_K−11_K) line emission shows that molecular gas is both expanding along the outflow direction following a Hubble law and rotating about the outflow axis, in agreement with the (3D) velocity field traced by methanol masers. The velocity field associated with rotation indicates a dynamical mass of ∼19 $M_\odot$ at the center of the core. The latter is likely to be concentrated in a single O9.5 ZAMS star, consistent with the estimated bolometric luminosity of G023.01−00.41. The physical properties of the CO (2–1) outflow emission, such as its momentum rate 6×10^{-3} $M_\odot$ km s^{-1} yr^{-1} and its outflow rate 2×10^{-4} $M_\odot$ yr^{-1}, support our estimates of the luminosity (and mass) of the embedded young stellar object.

Key words. ISM: kinematics and dynamics – instrumentation: high angular resolution – stars: individual: G23.01-0.41 – stars: formation

1. Introduction

The formation process of high-mass stars ($\gtrsim$10 $M_\odot$) still needs to be established. While theoretical models have been proposed, only recently substantial progress has been made observationally (see, e.g., Zinnecker & Yorke 2007). It is widely accepted that hot molecular cores (HMCs) are the sites where massive stars form, so it is of interest to study these objects at high angular resolution, through high-density tracers such as rare molecular species. In the recipe of star formation, a crucial role is played by disks and the associated jets/outflows, which in the case of high-mass stars might reduce the radiation pressure barrier on the infalling gas (i.e., the so-called flashlight effect) thus making accretion onto the protostar possible (see, e.g., Kuiper & Yorke 2013).

For these reasons, many observations have been devoted to HMCs and their molecular environment (e.g., Cesaroni et al. 2007, and references therein). The success of this type of study depends mostly on the selection of appropriate targets, since various facts may hinder the analysis of the velocity field inside the HMCs. For example, too long a distance makes the linear resolution insufficient to identify any putative disk in the HMC, while a suitable inclination with respect to the line of sight is needed to detect the velocity gradient owing to the outflow expansion and/or disk rotation. Multi-epoch VLBI observations of maser lines provide us with 3D information on the velocity field

⋆ Based on observations carried out with the Submillimeter Array. The Submillimeter Array is a joint project between the Smithsonian Astrophysical Observatory and the Academia Sinica Institute of Astronomy and Astrophysics and is funded by the Smithsonian Institution and the Academia Sinica.

⋆⋆ Final SMA and *Herschel* maps are only available at the CDS via anonymous ftp to cdsarc.u-strasbg.fr (130.79.128.5) or via http://cdsarc.u-strasbg.fr/viz-bin/qcat?J/A+A/565/A34

on scales as small as 10–100 AU and may be used to select promising objects for disk/outflow studies. With this in mind, we performed interferometric observations of dense gas and outflow tracers toward the high-mass star-forming region (HMSFR) G023.01−00.41. This star-forming site harbors a known HMC that we have recently studied by means of high-resolution maser observations, suggesting the presence of rotation and expansion within 2000 AU from the HMC center (Sanna et al. 2010, 2012).

G023.01−00.41 is a HMSFR located at a trigonometric distance of $4.59^{+0.38}_{-0.33}$ kpc (Brunthaler et al. 2009), which exceeds a bolometric luminosity of 10^4 $L_\odot$ (see Sanna et al. 2010, for a recent review). On a parsec scale, *Spitzer*/GLIMPSE images of the field reveal bright, "green fuzzy" emission at 4.5 μm, believed to be associated with an intense outflow activity (e.g., Cyganowski et al. 2009). Indeed, a massive ^{12}CO outflow has been detected with the IRAM interferometer at sub-pc scales (Furuya et al. 2008). Toward the center of the molecular outflow, emission from high-energy transitions of molecular species, such as CH_3CN and NH_3, has been detected, indicating the existence of a HMC hosting newly formed massive stars (Codella et al. 1997; Furuya et al. 2008). All the strongest maser species known to date have been detected from the HMC and subsequently imaged with multi-epoch VLBI observations (Sanna et al. 2010, 2012). We thus decided to perform Submillimeter Array (SMA) observations with subarcsec resolution to unveil the gas structure and kinematics in the HMC and associated outflow on scales ranging from 0.01 to 0.1 pc, with the aim of comparing these results to those obtained from the maser study.

This paper is organized as follows. In Sect. 2, we give the details of our SMA observations. In Sect. 3, we present the results of the analysis of selected molecular lines for typical HMC and outflow tracers. We also collect the photometric data at different IR wavelengthes at the position of G023.01−00.41, from several Galactic surveys available to date, and reconstruct its spectral energy distribution. In Sect. 4, we discuss the structure and velocity field of the region from the HMC to the outflow scale and the nature of the young stellar object(s) (YSOs) embedded in the HMC. Finally, the main results are summarized in Sect. 5.

2. Observations and calibration

The SMA observations toward G023.01−00.41 were conducted with the very extended (VEX) and compact array configurations and a single frequency setup in the 230 GHz band. The SMA receiver had two spectral sidebands each 4 GHz wide; the lower sideband (LSB) was set to include the CH_3CN (12_K–11_K) (from 220.747 GHz) and SiO (5–4) (at 217.104 GHz) lines, whereas the upper sideband (USB) was centered at the frequency of the ^{12}CO (2–1) transition (230.538 GHz). The correlator was configured to an almost uniform spectral resolution of 0.81 MHz (∼1.05 km s^{-1}) over the entire bandwidth, except for the spectral windows covering the strongest CH_3CN lines (K = 0–6) for which a resolution of 0.41 MHz (0.52 km s^{-1}) was used. The phase center of the observations was the putative position of the YSO inferred from masers and radio continuum observations (see Table 1; Sanna et al. 2010). Doppler tracking was performed assuming an LSR velocity of 77.4 km s^{-1}, corresponding to the rest velocity of the CH_3CN (6_K–5_K) lines (Furuya et al. 2008). More details on the observations are given in Table 1.

The visibility data were calibrated using the IDL MIR[1] package and were exported to the MIRIAD format for imaging. The

[1] The MIR cookbook is available at the following URL, https://www.cfa.harvard.edu/~cqi/mircook.html

Table 1. Summary of SMA observations (code 2009B–S032).

Obs. date	Array conf.	RA (J2000)	Dec (J2000)	Freq. cove. (GHz) LSB	Freq. cove. (GHz) USB	Spec. res. (MHz)	Bandpass cal.	Phase cal.	Flux cal.	*HPBW*
(1)	(2)	(3)	(4)	(5)	(6)	(7)	(8)	(9)	(10)	(11)
2010 Mar. 05	VEX (6)	$18^h34^m40\overset{s}{.}29$	−09°00′38″.3	216.9–220.9	228.9–232.9	0.81[a]	J1924−292	J1743−038 J1911−201	MWC 349	0″.4
2010 Apr. 28	Compact (8)	$18^h34^m40\overset{s}{.}29$	−09°00′38″.3	216.9–220.9	228.9–232.9	0.81[a]	3C 273 3C 454.3	J1743−038 J1911−201	Titan	3″.5

Notes. Column (1): observing dates. Column (2): array configurations and number of effective antennas. Columns (3)–(4): phase center of the observations. Columns (5)–(6): approximate ranges of rest frequencies covered in the lower and upper sidebands. Column (7): spectral resolution corresponding to a velocity width of 1.05 km s^{-1}. Columns (8)–(10): bandpass, phase, and absolute flux calibrators. Columns (11): approximate size of the beam obtained with a natural weighting at each configuration. [(a)] The spectral resolution was improved in the range 220.51−220.73 GHz by a factor of 2 to better sample the CH_3CN (12_K–11_K) lines (see Sect. 2).

Table 2. Observed lines.

ν (GHz)	Line	E_{low} (K)
217.105	SiO (5–4)	20.8
219.560	$C^{18}O$ (2–1)	5.3
220.399	^{13}CO (2–1)	5.3
220.476	CH_3CN (12_8–11_8)	515.0
220.486	$CH_3^{13}CN$(12_6–11_6)	313.9
220.532	$CH_3^{13}CN$(12_5–11_5)	235.8
220.539	CH_3CN (12_7–11_7)	408.0
220.570	$CH_3^{13}CN$(12_4–11_4)	171.9
220.594	CH_3CN (12_6–11_6)	315.3
220.600	$CH_3^{13}CN$(12_3–11_3)	122.2
220.621	$CH_3^{13}CN$(12_2–11_2)	86.7
220.634	$CH_3^{13}CN$(12_1–11_1)	65.3
220.638	$CH_3^{13}CN$(12_0–11_0)	58.2
220.641	CH_3CN (12_5–11_5)	236.8
220.679	CH_3CN (12_4–11_4)	172.6
220.709	CH_3CN (12_3–11_3)	122.6
220.730	CH_3CN (12_2–11_2)	86.8
220.743	CH_3CN (12_1–11_1)	65.4
220.747	CH_3CN (12_0–11_0)	58.3
229.589	CH_3OH (15_4–16_3)E	363.4
230.538	^{12}CO (2–1)	5.5

Notes. Values of frequencies and lower energies for each molecular transition are reported from the Cologne Database for Molecular Spectroscopy, CDMS (Müller et al. 2005).

compact and VEX array configurations had baselines ranging from 7 to 58 kλ (corresponding to spatial structures from 29.″5 to 3.″5), and from 82 to 390 kλ (i.e., from 2.″5 to 0.″5). The compact and VEX data were CLEANed together in order to retrieve information on both spatial scales. Maps were produced by varying the ROBUST parameter to find a compromise between angular resolution and sensitivity to extended structures. In the following, the resulting synthesized HPBW is reported in each figure. The continuum data were constructed from line free channels and then subtracted from the *uv*-data (MIRIAD task UVLIN). All the maps of the outflow tracers were obtained only from the compact configuration data to recover large-scale structures, with a ROBUST 0 weighting and a CELLSIZE of 0.″3. Further data analysis was performed with GILDAS[2].

3. Results

In the following, we describe the results of our SMA observations for selected molecular lines tracing the hot core and the molecular outflow (see Table 2), to analyze the dynamics (from 10^3 AU to several tenths of pc) of the gas associated with the radio continuum and maser source observed by Sanna et al. (2010). We also reconstruct the spectral energy distribution of G023.01−00.41 from the near-IR to the submm, using archival data.

3.1. Core tracers

Besides the dust continuum emission at 1.3 mm we have selected the strongest molecular lines detected with the VEX configuration to analyze the spatial distribution of the HMC emission. The overall results of these measurements are summarized in Table 3, together with the array configuration, the weighting used for the CLEANing algorithm, the restoring beam half-power width (HPBW), the position angle, and the rms of each map.

3.1.1. Dust continuum at 1.3 mm

The first line of Table 3 gives the integrated continuum flux density of the HMC at 1.3 mm, measured with the compact configuration of the SMA (∼0.3 Jy). We have not detected any other continuum source within a field of view of ∼1′ exceeding a flux density of ∼18 mJy beam^{-1} (3σ). For each array configuration, the continuum emission was fitted with a 2D Gaussian using the task IMFIT of MIRIAD. The peak position, intensity, flux densities, and deconvolved angular diameter obtained from the fit are reported in the last six columns of Table 3. A map of the dust continuum emission at 1.3 mm is presented in Fig. 1a and c, superimposed on the ammonia emission map in the (3, 3) inversion transition from Codella et al. (1997) and the map of the CH_3CN (12_2–11_2) line emission obtained by us.

3.1.2. CH_3CN (12_K–11_K) lines

The higher spectral resolution used for the CH_3CN J= 12–11 lines permits to accurately investigate the velocity field inside the HMC. The analysis presented in Figs. 2 and 3 was performed on the cube obtained from the combined dataset, cleaned with natural weighting (see Table 3).

CH_3CN (12_K–11_K) spectral analysis. To analyze the spectral profile of the methyl cyanide line, we use the CH_3CN spectrum obtained by averaging the emission inside the 5σ contour level of the continuum map (Fig. 2). Assuming that all K-components are excited within the same gas, we fitted the K = 0 to 4 components with five Gaussians forced to have same linewidths and with their separations in frequency fixed to the laboratory values. The K = 0 to 4 components were chosen because they are not significantly affected by line blending with other molecular species. The free parameters of the fit are the line intensities, the full width at half maximum (FWHM) of the lines, and the LSR velocity of an arbitrarily chosen K component. The results of the Gaussian fit are reported in Table 4. The assumptions appear to be justified a posteriori by the excellent agreement between the fit and the observed spectrum. To derive the physical parameters of the emitting gas, we also fitted the same spectrum with the XCLASS program (see Comito et al. 2005, and reference therein), which calculates the line profiles assuming local thermodynamic equilibrium for a given molecule column density, source size, and temperature. This time we fitted all the components up to K = 8. The peak velocity and FWHM were assumed equal to the values obtained from the Gaussian fit. In Fig. 2, we present the CH_3CN spectrum and the XCLASS fit (red profile) obtained by varying the source angular diameter, column density, and temperature. The best-fit parameters are given in Table 4. The green and blue profiles correspond, respectively, to the CH_3CN opacity and the $CH_3^{13}CN$ (12_K–11_K) spectrum computed with XCLASS for the same input parameters as used for CH_3CN and a relative abundance [CH_3CN]/[$CH_3^{13}CN$] = 20. The opacity profile demonstrates that the optical depth cannot be neglected to model the CH_3CN emission in G023.01−00.41, while the abundance ratio is significantly less than the expected value of 42 ± 13 (obtained from Wilson & Rood 1994 for a Galactocentric distance of 4.6 kpc), suggesting a significant enhancement of the $^{13}C/^{12}C$ ratio in the HMC. One sees some discrepancy between the fit and the observed spectrum for

[2] The GILDAS software is available at the following URL, http://iram.fr/IRAMFR/GILDAS/

Table 3. G023.01−00.41: core tracers.

							Peak position				Deconv. size	
Tracer	Array	Weight	*HPBW* & ($''$)	PA (°)	Image rms (Jy beam^{-1})	$\Delta V_{\rm LSR}$ (km s^{-1})	RA (J2000) (h m s)	Dec (J2000) (° ′ ″)	$F_{\rm peak}$ (Jy beam^{-1})	$F_{\rm int}$ (Jy)	$\theta_M \times \theta_m$ ($''$)	PA (°)
Dust 1.3 mm	Compact	NA	3.8 × 3.3	–15	0.006	...	18:34:40.284 (±0.″1)	–9:00:38.314 (±0.″1)	0.192 ± 0.010	0.294	3.4 × 1.9	–16
	Comb.	NA	0.97 × 0.94	25	0.004	...	18:34:40.292 (±0.″05)	–9:00:38.354 (±0.″05)	0.102 ± 0.008	0.209	1.20 × 0.60	–31.7
	VEX	UN	0.44 × 0.31	38	0.001	...	18:34:40.290 (±0.″01)	–9:00:38.183 (±0.″01)	0.035 ± 0.001	0.040	unresolved	
CH_3CN (12_K−11_K) data cube												
K-ladder[a]	Comb.	NA	1.12 × 1.07	–15	0.03	...	18:34:40.286 (±0.″02)	–9:00:38.374 (±0.″02)	1.57	...	...	...
CH_3CN (12–11) moment-0 maps												
K = 2	Comb.	UN	0.72 × 0.57	35	0.16[b]	75.6–81	18:34:40.286 (±0.″02)	–9:00:38.332 (±0.″02)	...	...	1.39 × 0.68	–19
K = 3	Comb.	UN	0.72 × 0.57	35	0.18[b]	75.6–81	18:34:40.288 (±0.″03)	–9:00:38.397 (±0.″03)	...	...	1.18 × 1.12	–50
K = 7	Comb.	UN	0.72 × 0.57	35	0.14[b]	75.6–81	18:34:40.287 (±0.″03)	–9:00:38.293 (±0.″03)	...	...	0.65 × 0.48	–49
K = 3 red	Comb.	UN	0.72 × 0.57	35	0.06[b]	81–83	18:34:40.294 (±0.″04)	–9:00:38.300 (±0.″04)	...	...	...	...
K = 3 blue	Comb.	UN	0.72 × 0.57	35	0.04[b]	73.6–75.6	18:34:40.270 (±0.″04)	–9:00:38.230 (±0.″04)	...	...	...	...
CH_3OH (15_4–16_3) E maps												
CH_3OH[c]	Comb.	R0	0.71 × 0.58	47	0.03	...	18:34:40.291 (±0.″02)	–9:00:38.250 (±0.″02)	0.264 ± 0.013	0.520	0.85 × 0.34	–33
CH_3OH red	Comb.	R0	0.71 × 0.58	47	0.07[b]	79.4–81.6	18:34:40.289 (±0.″04)	–9:00:38.440 (±0.″04)	...	...	...	...
CH_3OH blue	Comb.	R0	0.71 × 0.58	47	0.08[b]	73.9–76.1	18:34:40.289 (±0.″04)	–9:00:38.160 (±0.″04)	...	...	...	...

Notes. Column (1): molecular tracer. Column (2): array configurations; "Comb." stands for the combined imaging of the Compact and VEX data. Columns (3)–(5): image weighting, synthesized beam, and position angle (east of north) of each map. Column (6): 1σ rms of the map. Column (7): integrated velocity ranges (see Sect. 3.1). Columns (8)–(9): for maps of dust emission and lines measured within the bulk emission (Sect. 3.1), the peak position was derived by an elliptical Gaussian fitting (with fitted errors). For those line maps integrated over the red- and blue-shifted emission, we give the position of the peak. Column (10): peak brightness derived by Gaussian fitting (with fitted errors). Column (11): total integrated flux of the emission within the 5σ contour level. Columns (12)–(13): deconvolved major, minor axes and position angle of the emission derived by Gaussian fitting. [(a)] The absolute peak position and its intensity correspond to the component K = 1. [(b)] Units of Jy beam^{-1} km s^{-1}. [(c)] Channel map at the systemic velocity of the HMC (78.3 km s^{-1}).

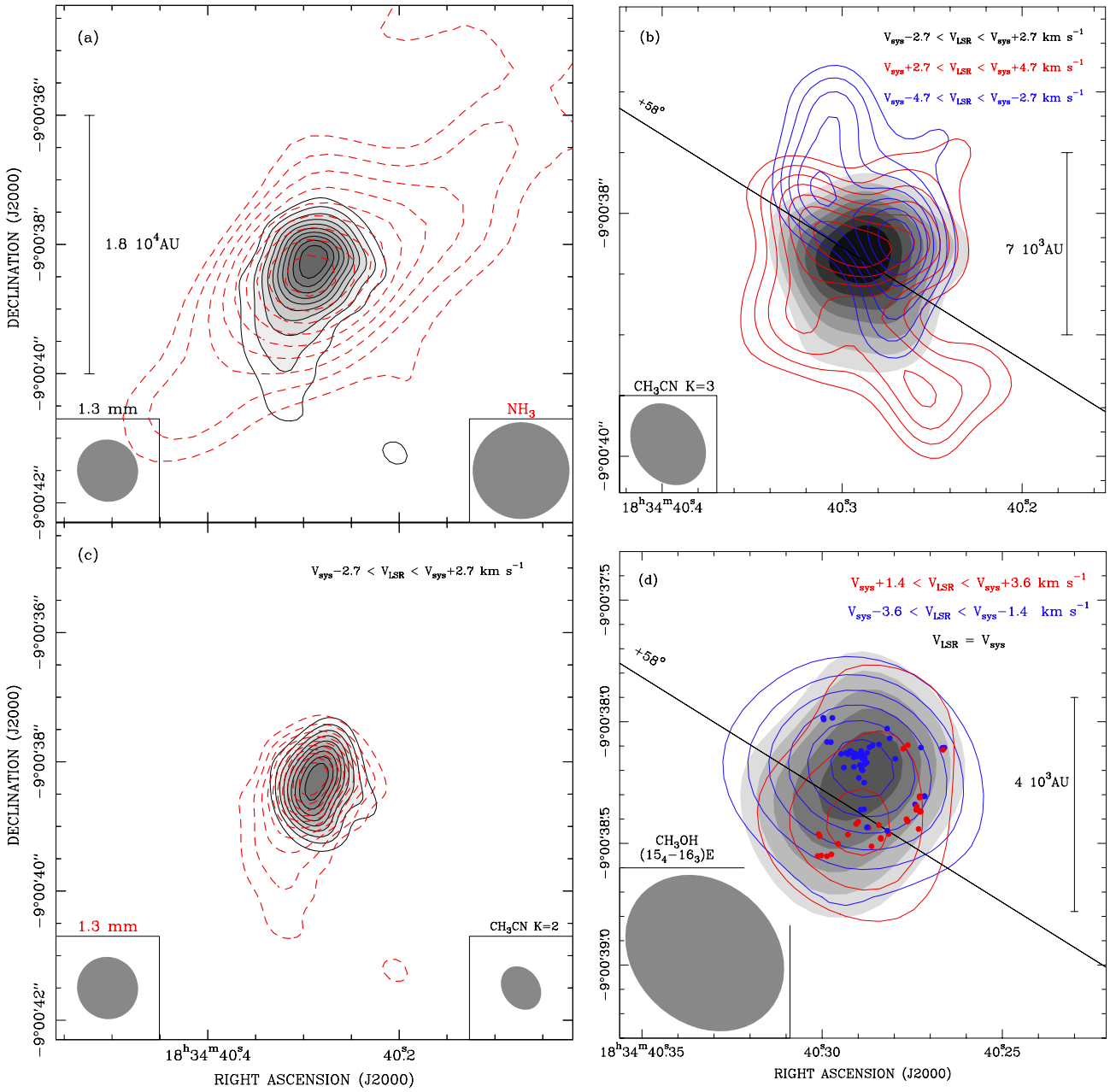

Fig. 1. Images of the hot molecular core. **a)** SMA map of the 1.3 mm continuum emission from the combination of the compact and VEX configurations (grayscale), superimposed on the VLA–C NH_3 (3, 3) map obtained by Codella et al. (1997, dashed red contours). Contour levels start from 5σ by 3σ for the 1.3 mm map (details on Table 3) and from 3σ in steps of 1σ (4 mJy beam^{-1}) for the NH_3 (3,3) map. The SMA and VLA–C synthesized beams are shown in the lower left and right corners, respectively. The linear scale is shown for comparison with panels **b)** and **d)** as well. **b)** Maps of the CH_3CN (12_3–11_3) line integrated over its FWHM in three velocity ranges reported on top of the panel (V_{sys} = 78.3 km s^{-1}; see Sect. 3.1). Contours start at 3σ and increase in steps of 1σ. The SMA synthesized beam is shown in the lower left corner (Table 3). The NE–SW line shows the outflow direction as described in Sect. 4.2. The f.o.v. is two times smaller than in panel **a)**. **c)** Similar to panel **a)** with superimposed a map of the CH_3CN (12_2–11_2) line (gray contours) integrated over the same bulk emission as panel **b)**. The K = 2 line contours start at 3σ and increase in steps of 1σ. The SMA synthesized beam is shown in the lower right corner (Table 3). **d)** Maps of the CH_3OH ($15_4 - 16_3$)E line emission, the strongest observed in the VEX configuration. Gray, blue, and red contours are, respectively, maps of emission at the systemic velocity, and in the blue- and redshifted wings of the line (the velocity ranges are indicated in the upper right corner). Gray contours start at 3σ and increase in steps of 1σ, whereas the blue and red contours start at a 5σ level in steps of 2σ. The SMA synthesized beam is shown in the lower left corner (Table 3). Blue and red dots mark the positions of the blue- and redshifted methanol maser spots detected by Sanna et al. (2010). The NE–SW line is the same as in panel **b)**. The f.o.v. is four times smaller than in panel **a)**.

the K = 0 and 1 lines: this could be caused by extended emission in the lower excitation transitions (K = 0 and 1), which is not considered in the model fit, since the latter assumes the same source size for all K components. Also, we explicitly note that the higher excitation lines of the $CH_3^{13}CN$, which are not reproduced well by the XCLASS fit, are below the sensitivity limits of our spectrum.

$CH_3CN(12_K$–$11_K)$ velocity field. In the following, we assume that the peak velocity of the CH_3CN (12_K–11_K) lines of 78.3 km s^{-1} is the systemic velocity of the HMC (V_{sys}).

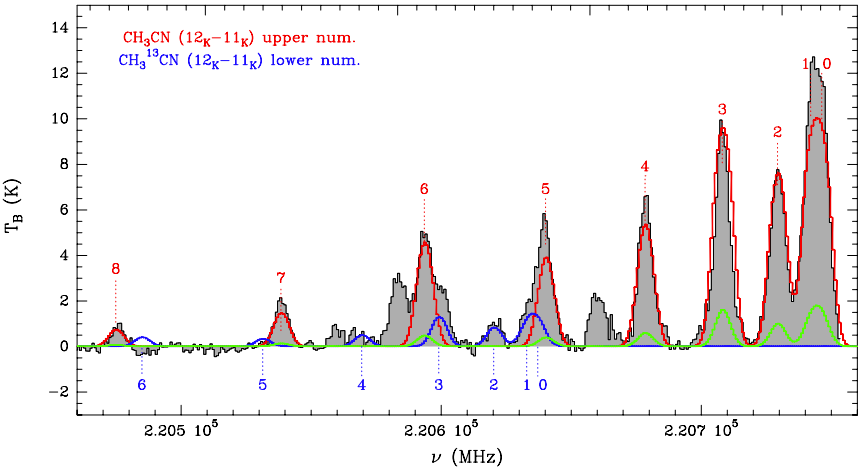

Fig. 2. Spectra of the $CH_3CN\,(12_K{-}11_K)$ lines computed within the 5σ contours of the dust continuum map (see Sect. 3.1) up to the higher component detectable ($K = 8$). The gray profile shows the integrated spectrum and compares the measured profile and the XCLASS synthetic spectra obtained in LTE approximation for: 1) the CH_3CN K-ladder (red); 2) the $CH_3^{13}CN$ K-ladder (blue); 3) and the opacity profile (green; same scale as the intensity one). The position of the K-ladders for the CH_3CN and its isotopomer is marked. Details in Sect. 3.1 and Table 4.

Table 4. Results of the $CH_3CN\,(12_K{-}11_K)$ spectra analysis.

K-component	V_{LSR} (km s^{-1})	Δv (km s^{-1})	$\int T_B dv$ (K km s^{-1})
$K = 0$	78.34 ± 0.04	9.43 ± 0.05	62 ± 1
$K = 1$			63 ± 1
$K = 2$			66.4 ± 0.8
$K = 3$			69.2 ± 0.8
$K = 4$			45.7 ± 0.8
XLCASS synthetic spectrum:			
Source size (diameter): 1.2 arcsec			
Rotational temp.: 195 K			
Column density: 5.1×10^{16} cm^{-2}			

Notes. Properties of the $CH_3CN\,(12_K{-}11_K)$ line emission. We list the centroid velocity, line width (FWHM), and line intensities from the multiple-Gaussian fitting, and the best-fit parameters obtained with XCLASS (details on Sect. 3.1 and Fig. 2).

In Fig. 1b, we present a map of the emission from the $K = 3$ transition within the line FWHM ($V_{sys} \pm 4.7$ km s^{-1}), sampled in three velocity intervals. These intervals were selected to analyze the velocity structure of the core. In particular, a map of the bulk emission was obtained by averaging the emission over the interval $V_{sys} \pm 2.7$ km s^{-1}(see also Fig. 3a), while for the maps of the blue- and redshifted emission we chose the velocity intervals between $V_{sys} \pm 2.7$ km s^{-1} and $V_{sys} \pm FWHM/2$. Figure 1b shows that the blue and red contours outline a NE–SW bipolar structure centered on the peak of the bulk emission (gray scale) and consistent with that of the bipolar outflow mapped by Furuya et al. (2008). However, on a smaller scale the blue- and redshifted emissions appear to rotate by 90°, thus tracing a velocity gradient along the SE–NW direction.

This is illustrated better in Fig. 3a, where we present a CH_3CN velocity map obtained by fitting the $K = 3$ line with a Gaussian at each point of the map. Only points with emission above 7σ have been considered. This map is consistent with the one obtained from the line wings, since the velocity gradient seems to define two directions: in fact, the redshifted gas is found both to the SE and to the SW, while the blueshifted emission peaks to the NE and NW. The core appears elongated in the SE–NW direction, as also shown by the continuum map in Fig. 1a. We have computed the position–velocity (p–v) plot of the CH_3CN $K = 3$ line along the major axis of the core as defined by the dust continuum emission, namely along a PA = −32° (see Fig. 3b). This confirms the existence of a velocity gradient and presents two peaks symmetrically displaced with respect to the center of the plot, as defined by the position of the continuum peak and the systemic velocity.

Complementary information is obtained by fitting the emission in each channel (i.e., at fixed velocity) of the $K = 0$ to 4 lines, with a 2D Gaussian. Only channels where the emission was above 7σ were used. The peak positions orthogonally projected along the two directions with PA = 58° and PA = −32° are plotted as a function of the corresponding velocity in Fig. 3c and d. The uncertainty of the peak position (±0.05″) has been estimated as the Gaussian fit uncertainty for a typical signal-to-noise ration of 10 in each channel map. We then performed a linear fit to the peak distributions; the corresponding slopes (dv/dx) and correlation coefficients (r) are, respectively, −22.4 ± 2.4 km s^{-1} arcsec^{-1}, 0.8 for PA = 58° and −17.2 ± 3.3 km s^{-1} arcsec^{-1}, 0.6 for PA = −32°. In Fig. 3d we only fitted the points lying within the FWHM (dashed red and blue lines) of the CH_3CN lines. Out of this range (corresponding to distances greater than about 0.″2 from the dust continuum peak) the points seem to converge towards 0 offset (see discussion in Sect. 4.1). For comparison, in Figs. 3c and d we also report the positions of the 6.7 GHz CH_3OH masers as measured by Sanna et al. (2010). These maser points were not considered in the linear fits.

3.1.3. $CH_3OH\,(15_4{-}16_3)E$ line

The $15_4{-}16_3$ methanol line was selected as the highest excitation ($E_{low} \approx 363$ K) and strongest transition visible in the VEX data, with the aim to compare the thermal methanol emission with the 6.7 GHz methanol maser emission studied by Sanna et al. (2010). The line profile (Fig. 4) presents two peaks at about $V_{sys} \pm 2.5$ km s^{-1}, with the blueshifted peak brighter than the redshifted one by a factor of almost 2, and a similar FWHM of about 3 km s^{-1} for both components. This asymmetry is still present in the low-resolution spectrum obtained with the compact configuration. The origin of this spectral profile is discussed in Sect. 4.1.1. In Fig. 1d, we show the spatial distribution of different velocity components of the methanol gas. The CH_3OH emission was integrated over three velocity ranges: a map of the blueshifted emission centered on $V_{sys} - 2.5$ km s^{-1} and integrated over its FWHM, corresponding to three velocity channels (blue contours); a map of the redshifted emission centered at V_{sys}+2.5 km s^{-1} and integrated over the same blueshifted linewidth (red contours); a channel map of the emission at the systemic velocity of the core (gray scale). In Table 3 we list the

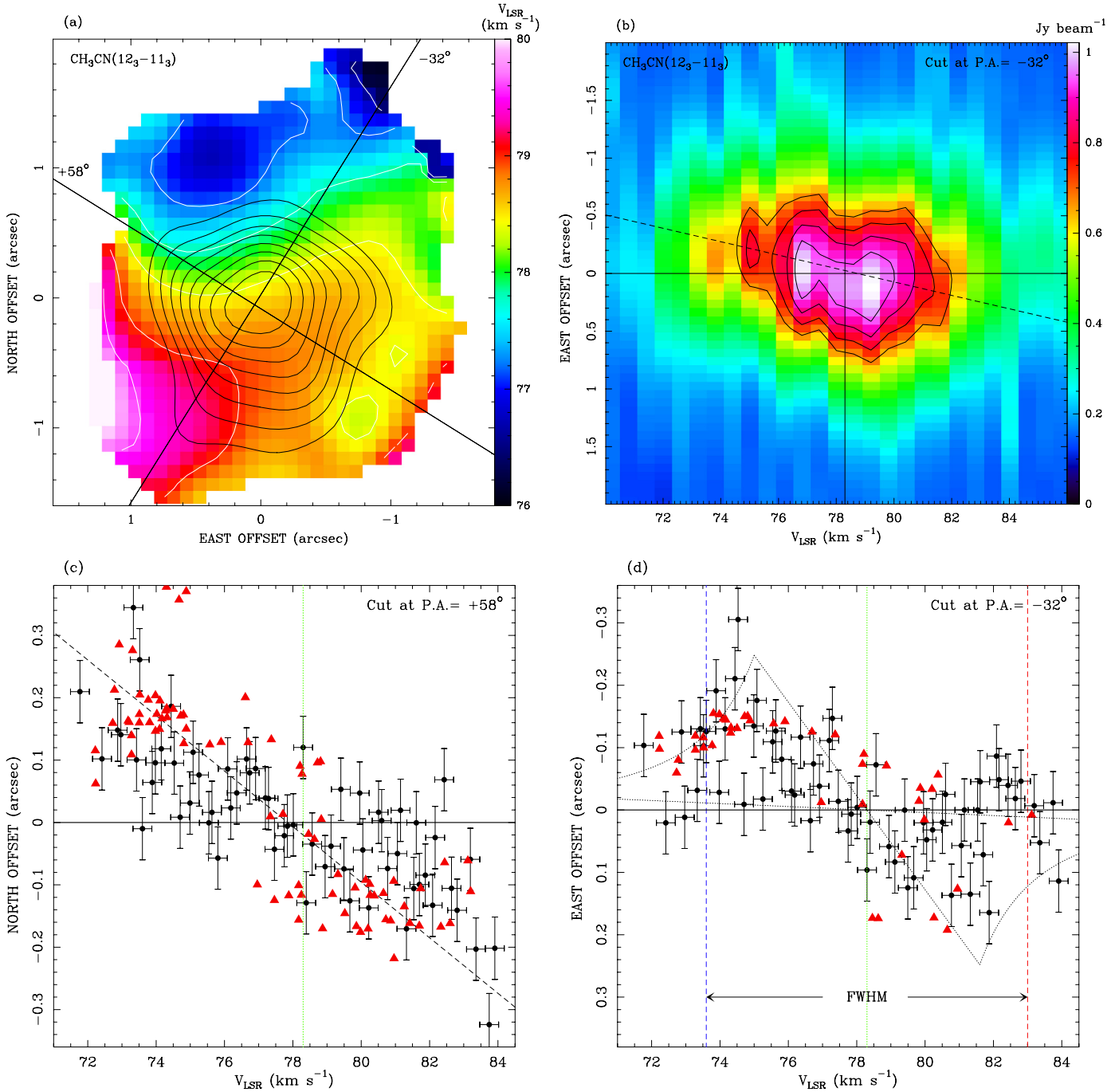

Fig. 3. Velocity pattern of the inner core from the CH_3CN (12–11) lines. In all panels the vertical and horizontal lines mark, respectively, the systemic velocity of the core and the position of the dust continuum peak. **a)** Map of the CH_3CN (12_3−11_3) line velocity (color scale). Offsets are measured with respect to the phase center. Superimposed are the contours of the bulk emission from Fig. 1b (black) and the directions (straight lines), passing through the continuum peak, along which the $p-v$ cuts presented in the following panels have been computed. **b)** $p-v$ cut of the CH_3CN (12_3−11_3) line along the major axis of the elongated HMC (−32°); east offsets are measured along this cut. Contours start at 60% of the peak emission and increase by 10% steps; colors are drawn according to the wedge on the right side. The dashed line represents the linear fit performed in panel **d)** within the FWHM of the CH_3CN (12_K−11_K) lines. **c)** $p-v$ distribution of the peaks of the CH_3CN emission (black dots) at different velocities (only the $K = 0$ to 4 components have been used) along the outflow direction (+58°); north offsets are measured along this cut. Error bars indicate the spectral resolution of the CH_3CN (12–11) observations and the uncertainty of the Gaussian fits in the maps. The dashed black line is the best linear fit to the peak distribution, which has a slope $dv/dx = -22.4 \pm 2.4$ km s^{-1} arcsec^{-1}, and a correlation coefficient of $r = 0.8$. The red triangles represent the CH_3OH maser spots detected by Sanna et al. (2010). **d)** Same as panel **c)** for the cut along the major axis of the elongated HMC (PA = −32°); east offsets are measured along this cut. The vertical dashed lines mark the limits of the FWHM of the CH_3CN (12–11) lines. The best linear fit (not shown in this figure) to the points within the line FWHM is obtained for $dv/dx = -17.2 \pm 3.3$ km s^{-1} arcsec^{-1}, with $r = 0.6$. The dotted pattern encompasses the region where emission is expected from a Keplerian disk rotating about a 19 $M_\odot$ star. Here, the red triangles mark only the CH_3OH maser spots with a distance of less than 0.25 arcsec from the dust continuum peak.

Table 5. G023.01−00.41: properties of the molecular outflow.

Tracer	Lobe	R (pc)	t_{dyn} (yr)	M_{out} ($M_\odot$)	$\dot{M}_{out}$ ($M_\odot$ yr^{-1})	p ($M_\odot$ km s^{-1})	$\dot{p}$ ($M_\odot$ km s^{-1} yr^{-1})	E_{mec} (10^{46} erg)	L_{mec} ($L_\odot$)
^{12}CO	Red–A	0.51	3.4×10^4	2.5	0.8×10^{-4}	37.5	1.1×10^{-3}	0.6	1.4
	Blue–A	0.44	2.9×10^4	1.4	0.5×10^{-4}	20.5	0.7×10^{-3}	0.3	0.9
SiO	Red–A	0.13	5.5×10^3	1.0	1.8×10^{-4}	23.1	4.2×10^{-3}	0.5	7.9
	Blue–A	0.12	5.1×10^3	0.6	1.3×10^{-4}	14.9	2.9×10^{-3}	0.3	5.5
		$R \times \frac{1}{\cos\ 30^\circ}$	$t_{dyn} \times \tan\ 30^\circ$	M_{out}	$\dot{M}_{out} \times \cot 30^\circ$	$p \times \frac{1}{\sin\ 30^\circ}$	$\dot{p} \times \frac{\cos\ 30^\circ}{\sin^2\ 30^\circ}$	$E_{mec} \times \frac{1}{\sin^2\ 30^\circ}$	$L_{mec} \times \frac{\cot 30^\circ}{\sin^2\ 30^\circ}$
^{12}CO		0.55	1.8×10^4	4.0	2.2×10^{-4}	116	6.2×10^{-3}	3.6	16
SiO		0.14	3.1×10^3	1.6	5.4×10^{-4}	76	2.4×10^{-2}	3.2	92

Notes. Properties of the molecular outflow estimated from the integrated emission in Fig. 5 (see details in Sect. 3.2). Values not corrected for inclination are given for each lobe separately and are the following: the maximum length of the outflow lobe (R); the dynamical time scale (t_{dyn}); the outflow lobe mass and the associated outflow rate (M_{out} & $\dot{M}_{out}$); the momentum and mechanical force (p & $\dot{p}$); the mechanical energy and luminosity (E_{mec} & L_{mec}). The last two lines give the total outflow parameters, corrected for an inclination angle of 30° with respect to the plane of the sky.

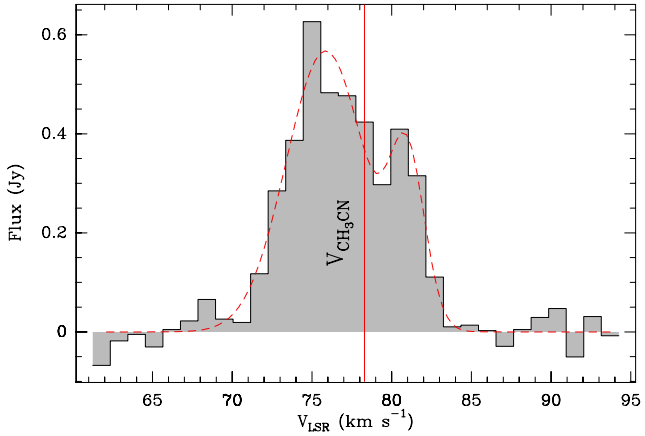

Fig. 4. Spectrum of the CH_3OH (15_4-16_3)E line emission presented in Fig. 1d. The dashed red line in the spectrum draws a double Gaussian fitting to the blue- and redshifted wings of the CH_3OH profile, symmetric with respect to the systemic velocity of the CH_3CN lines (vertical red line).

parameters obtained with a 2D Gaussian fit, for the methanol emission at the systemic velocity.

3.2. Outflow tracers

3.2.1. ^{12}CO (2−1) line and isotopomers

The CO emission from the J= 2–1 rotational transition is spread over a radius of about 30″ around the dust continuum peak (Fig. 5a–c), consistent with the findings of Furuya et al. (2008) for the ^{12}CO(1–0) transition (their Fig. 6a–c). We restrict our analysis to the emission inside the dashed box in Fig. 5a, which matches the J = 1–0 emission detected with the IRAM interferometer better. Our CO maps reveal the presence of a second source of CO emission (clump "B" in Fig. 5a) offset by about 25″ to the SW of the HMC. The LSR velocity range of the CO emission from the HMC extends up to ±30 km s^{-1} from V_{sys}, as shown in Fig. 6, whereas at more blueshifted velocities, the spectrum is affected by the emission from clump B. In Sect. 4.2, we conclude that clump B is an unrelated cloud lying along the line-of-sight, and as such it will not be discussed any further.

To adopt suitable velocity ranges to identify the blue- and redshifted outflow emission, we set the inner limits of the line wings at $V_{sys} \pm FWHM/2$, where FWHM is the CH_3CN linewidth. This assumption is supported by the tendency at higher velocities for the CH_3CN gas to align with the outflow direction (see Fig. 3d). These limits correspond to ±4.7 km s^{-1} from the systemic velocity. As terminal velocities of the flow (V_t), we have assumed the velocities where the wing emission falls below the 3σ level (i.e., at 49 km s^{-1} and 108 km s^{-1}, respectively). After decreasing below the 3σ level at V_{sys} − 18.7 km s^{-1} (i.e., at 59.6 km s^{-1}), the blueshifted emission is detected again at higher velocities up to the same (in absolute value) redshifted terminal velocity ($|V_t - V_{sys}|$ = 29.7 km s^{-1}). These terminal velocities correspond to the maximum velocities measured by Furuya et al. (2008) for the ^{12}CO (1–0) and ^{13}CO (1–0) line emission. In Fig. 5c, we show the bulk C^{18}O (2–1) line emission averaged over the FWHM of the CH_3CN lines, for comparison with Fig. 6c of Furuya et al. (2008). In Figs. 8 and 9, channel maps of the blue- and redshifted wings of the ^{12}CO (2–1) and ^{13}CO (2–1) emission are shown in pairs of channels equally offset (in absolute value) from the systemic velocity.

The physical properties of the ^{12}CO (2–1) outflow are reported in Table 5 for the blue- and redshifted lobes separately (following, e.g., Cabrit & Bertout 1990; Beuther et al. 2002). The length of each CO lobe was calculated from the peak of the dust continuum map to the farthest CO emission detected along the NE–SW direction (plus signs in Fig. 5a). Since the spatial distribution of the CO gas shows a clumpy morphology (e.g., Fig. 8), and the maximum outflow velocity does not increase linearly as a function of the distance from the HMC, the outflow properties are estimated for a median velocity of 15 km s^{-1}. For calculating the CO outflow mass, we made use of the first equation in Sect. 3.2.2 of Qiu et al. (2009), assuming an excitation temperature of 30 K and a ^{12}CO abundance relative to H_2 of 10^{-4}. The excitation temperature was adopted for comparison with the SiO outflow properties (see below). Decreasing the excitation temperature by a factor 2, for consistency with T_{ex} = 15 K adopted by Furuya et al. (2008), reduces the outflow mass estimates by less than a factor 1.3. We applied a constant correction for the ^{12}CO opacity (τ_{12}) of 5.3, derived from the second equation in Sect. 3.2.2 of Qiu et al. (2009) for a ^{12}CO/^{13}CO abundance ratio of 42 (from Wilson & Rood 1994).

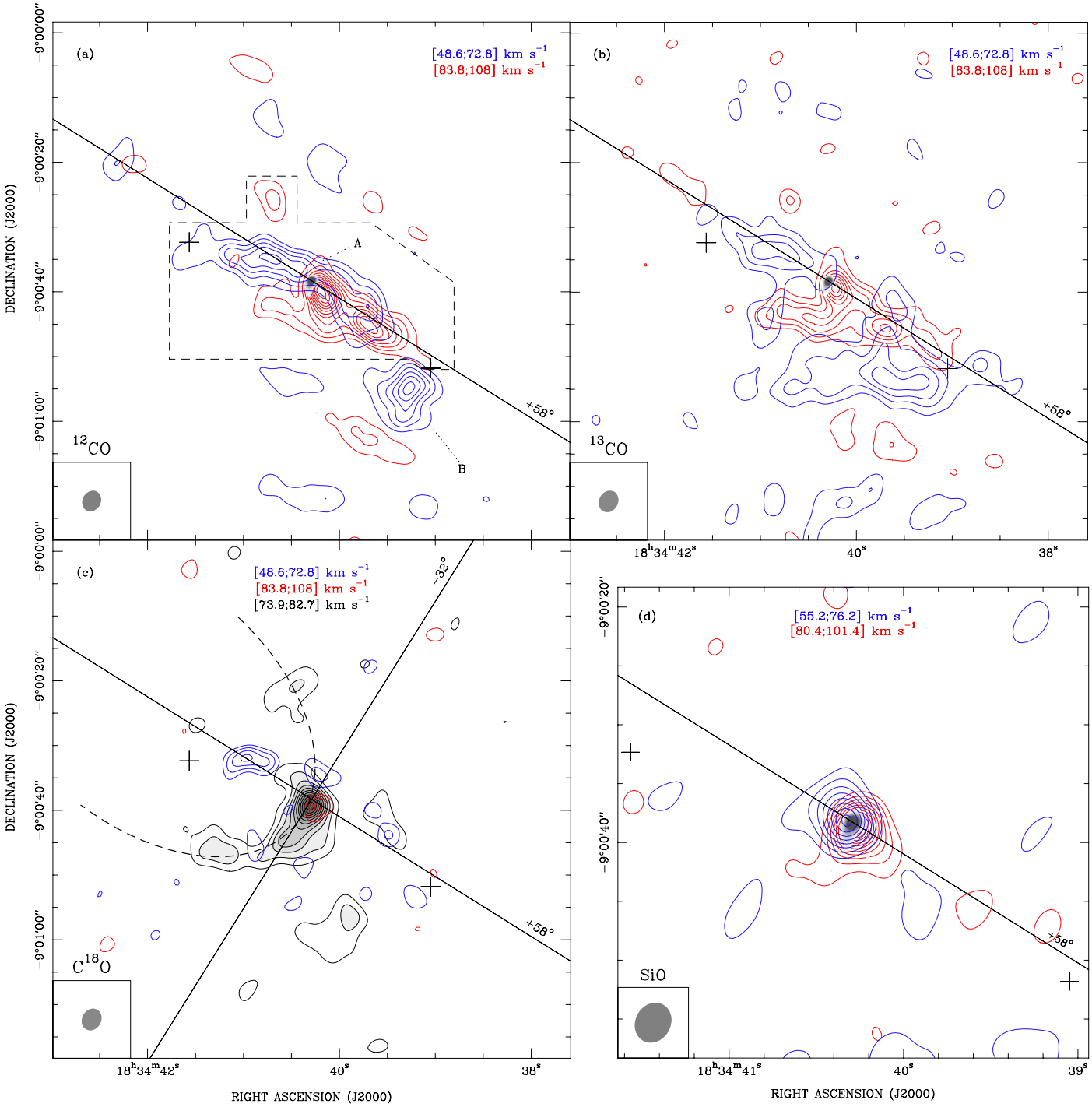

Fig. 5. SMA maps of the outflow emission from G023.01−00.41. **a)** Integrated emission of the ^{12}CO (2–1) line within the velocity ranges indicated in the top right corner. The blue and red velocities are symmetric with respect to the V_{sys} of the HMC. Contours start at 3σ and increase in steps of 2σ (corresponding to 3.8 and 2.6 Jy beam^{-1} km s^{-1}, for the red- and blueshifted wings, respectively). At the center of the field is the 1.3 mm continuum map (grayscale). The NE–SW line draws the direction of the outflow inferred from the analysis of the HMC tracers (at +58°). Labels A and B indicate, respectively, the HMC and another CO clump probably lying along the line of sight (see Sect. 4.2). The two plus signs mark the reference points for the computation of the outflow length (details in Sect. 3.2). The dashed pattern outlines the region over which emission was averaged to obtain the spectra in Fig. 6. The SMA synthesized beam is shown in the lower left corner. **b)** Same as panel **a)**, for the ^{13}CO (2–1) line emission. Contours start at 3σ and increase in steps of 2σ (corresponding to 0.61 and 0.82 Jy beam^{-1} km s^{-1}, for the red- and blueshifted emission, respectively). **c)** Same as panel **a)**, for the C^{18}O (2–1) line emission. The gray contours are a map of the C^{18}O bulk emission integrated over the FWHM of the CH_3CN lines. The NW–SE line indicates the direction of the major axis of the HMC and the dashed pattern marks the putative border of the NE outflow lobe, partially traced by the C^{18}O bulk emission. Contours start at 3σ and increase in steps of 2σ (0.59 Jy beam^{-1} km s^{-1}) for the bulk emission, and of 1σ for the redshifted (0.28 Jy beam^{-1} km s^{-1}) and blueshifted (0.33 Jy beam^{-1} km s^{-1}) emission. **d)** Similar to panel **a)** but for the SiO (5–4) line emission and with a zoom of two times the field of view. Contours start at 3σ and increase in steps of 2σ (0.64 and 0.54 Jy beam^{-1} km s^{-1} for the red- and blueshifted emission, respectively).

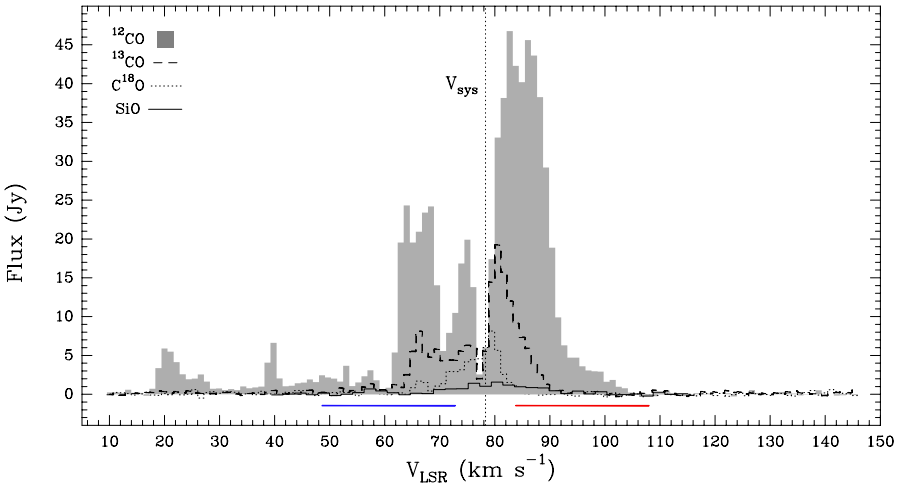

Fig. 6. Spectra of the outflow tracers, ^{12}CO (2–1), ^{13}CO (2–1), C^{18}O (2–1), and SiO (5–4) obtained by averaging the emission inside the dashed box in Fig. 5a. The ranges of integration used for the CO lines are marked along the *x*-axis (blue and red lines); the rest velocity of the CH_3CN (12–11) lines is also shown (V_{sys}).

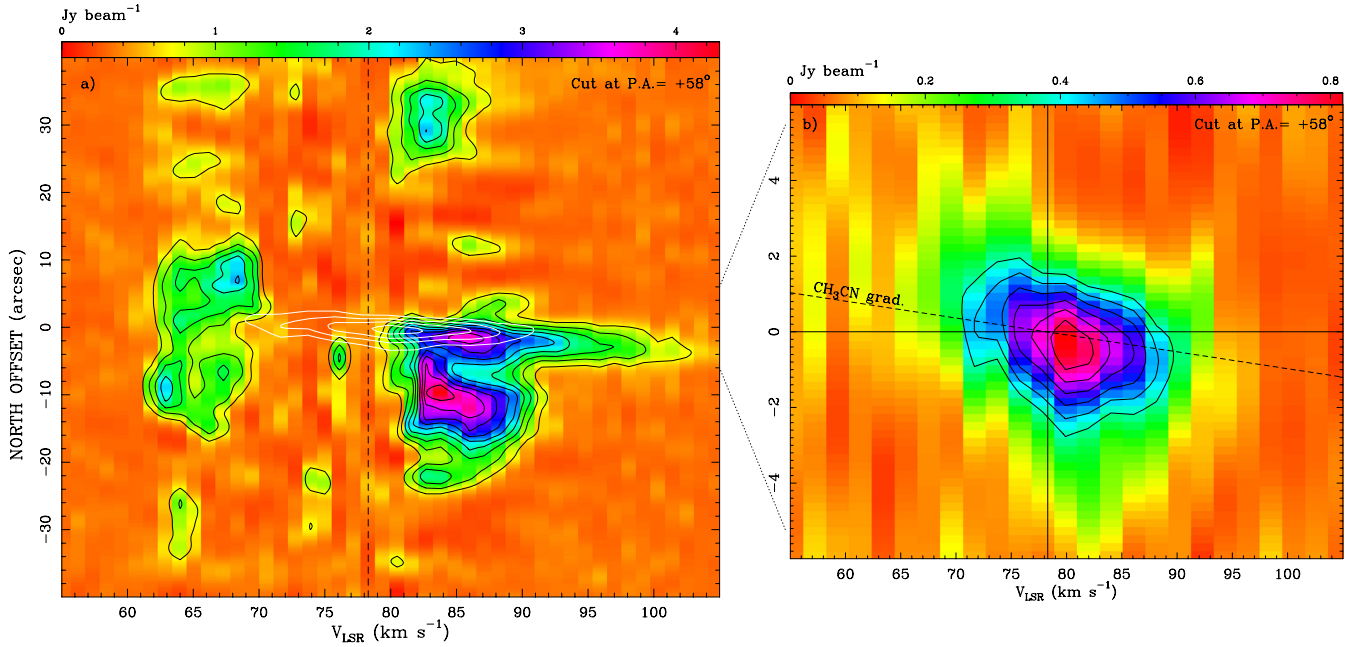

Fig. 7. $p-v$ plot of the outflow tracers ^{12}CO (2–1) and SiO (5–4), along a cut with PA = +58° (cf. Fig. 5a and d). The vertical line marks the V_{sys}. **a)** The ^{12}CO emission is drawn with colors (color scale on top) and black contours, from 10% of the peak emission increasing by steps of 10%. A map of the SiO emission is overlaid in white contours starting from 30% of the peak emission and increasing by 20% steps. **b)** Close-up view of the SiO $p-v$ plot within 6″ from the HMC. The SiO emission is drawn with colors (color scale on top) and black contours, from 40% of the peak emission increasing by steps of 10%. The dashed line denotes the velocity trend obtained from the CH_3CN emission (Fig. 3c).

This average optical depth was derived from the flux density ratio between the redshifted outflow lobes of Fig. 5a and b (within the 3σ level of the ^{12}CO emission), where the ^{12}CO and ^{13}CO gas components are well matched in position. When assuming the same ^{12}C/^{13}C abundance ratio (~20) as obtained for the HMC from the CH_3CN and $CH_3^{13}CN$ molecules, the outflow mass estimates are reduced by a factor 2.

In Fig. 7a, we also present a $p-v$ plot of the ^{12}CO (2–1) emission along a position angle of +58° passing through the peak of the continuum emission. The CO emission was averaged over a strip about 2″ wide from each side of the cut, in order to include most of the emission from the outflow lobes. We comment on the outflow from G023.01−00.41 further in Sect. 4.2.

3.2.2. SiO (5–4) line

The emission from the J = 5–4 line of the SiO molecule arises from a region of 6.″7 (0.15 pc) around the dust continuum peak and covers the velocity range $V_{sys} \pm 23.1$ km s^{-1} (Figs. 5d and 6). These limits correspond to the velocities of the channel maps where the emission from both the blue- and redshifted wings drops below the 3σ level. The SiO molecule is almost exclusively associated with high velocity gas, and its gas-phase abundance is greatly enhanced by strong shocks passing through dense molecular gas (and disrupting dust grains). Therefore, we integrated the SiO emission starting from the spectral channels next to the systemic velocity (Fig. 5d).

The physical properties of the SiO outflow are reported in Table 5 for the blue- and redshifted lobes separately. The length of the SiO lobes was calculated from the peak of the dust continuum map to the farthest (3σ contours) SiO emission along a direction with PA = +58° (black line in Fig. 5d). The outflow velocity used for these estimates is the maximum line-of-sight velocity observed (i.e., 23.1 km s^{-1}). For calculating the SiO outflow mass, we used Eq. (1) of Gibb et al. (2004), assuming an excitation temperature equal to the energy of the J = 5 level

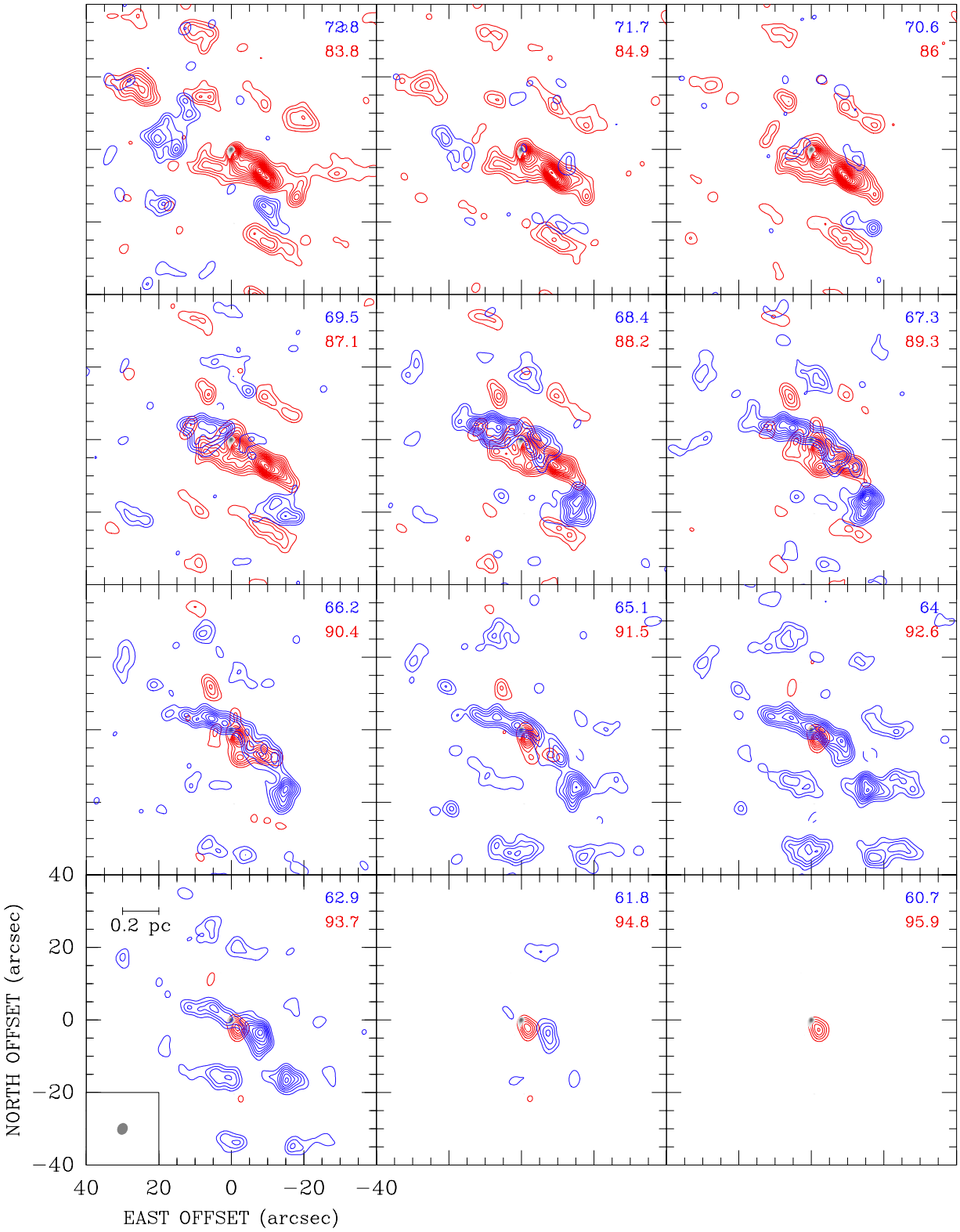

Fig. 8. Channel maps of the ^{12}CO (2–1) line emission observed with the compact configuration of the SMA. Each box contains pairs of maps corresponding to the blue- and red-shifted emission at the same velocity offset from V_{sys}. The corresponding LSR velocities (km s^{-1}) are indicated in the top right corner of each box. Contours start from a 3σ level of 0.4 Jy beam^{-1} for both wings and increase in steps of 2σ. In the *bottom left panel*, a linear scale and the synthesized beam are shown. The map of the 1.3 mm dust continuum (gray contours) is shown in overlay.

(i.e., 31 K), and an SiO abundance relative to H_2 of 2×10^{-9} (Gibb et al. 2007). It is worth noting that both the SiO outflow velocity and the excitation temperature are probably lower limits as are the inferred quantities. Also, we explicitly note that the SiO abundance is still affected by large uncertainties (e.g., Gibb et al. 2007). In Fig. 7b, we present a $p - v$ plot of the SiO (5–4) emission close to the HMC along a cut at PA = +58°, for comparison with the velocity gradient observed in CH_3CN.

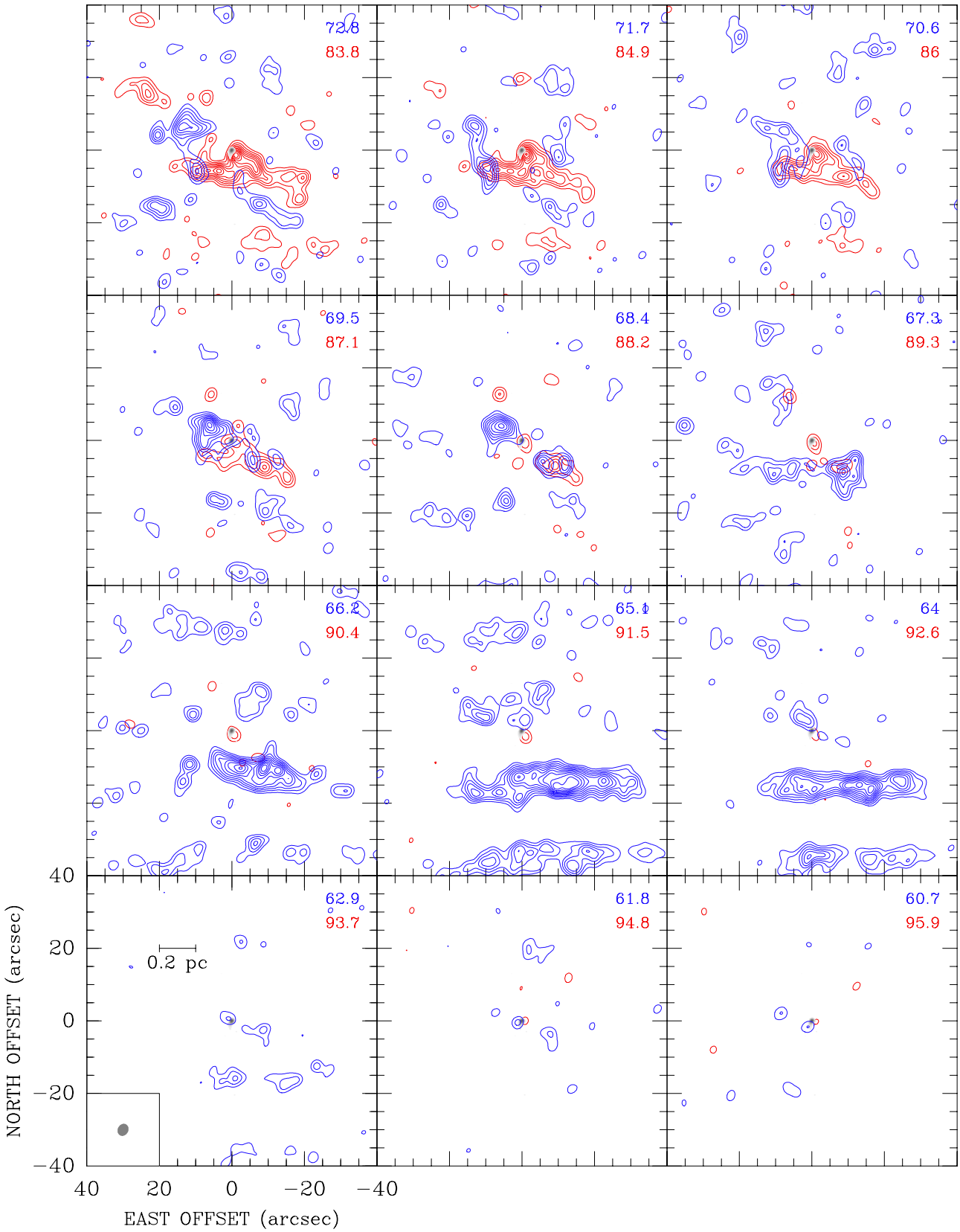

Fig. 9. Same as Fig. 8 but for the ^{13}CO (2–1) line emission. Contours start from a 3σ level of 0.14 Jy beam^{-1} and increase in steps of 2σ.

In Fig. 7a, the same p–v plot (white contours) is superimposed on the one inferred from the ^{12}CO (2–1) line.

We conclude that the SiO outflow morphology and physical parameters are consistent with those obtained from the CO isotopomers, within the uncertainties.

3.3. Spectral energy distribution

Table 6 lists the flux densities from 3.4 μm to 1.1 mm toward G023.01−00.41 obtained from the *Herschel* Infrared Galactic Plane Survey (Hi-GAL; Molinari et al. 2010) images

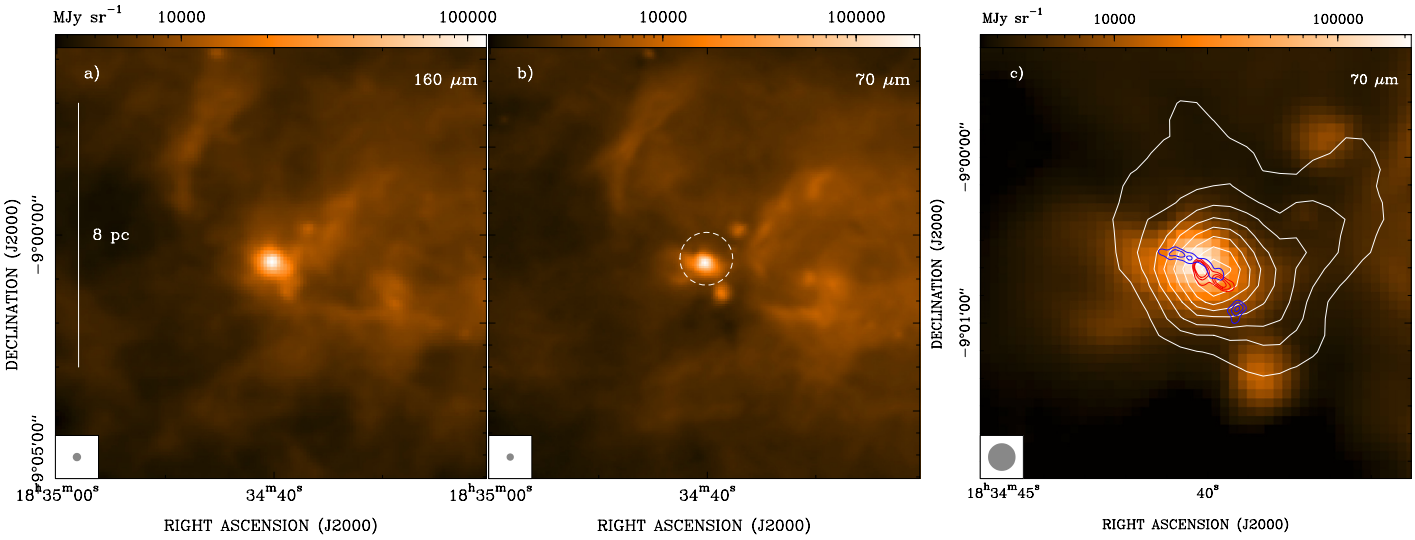

Fig. 10. Parsec-scale structure of the G023.01−00.41 star forming region obtained at 160 μm and 70 μm (color log-scale on top of each panel), and at 870 μm (gray contours, panel **c)**). All plots are centered on the HMC, as done in Figs. 1 and 5. **a)** *Herschel* view of the region at 160 μm within ±4.9′ from the HMC. The linear scale is drawn on the left side of the plot. **b)** Similar to **a)** but for the 70 μm continuum emission. The dashed white circle marks the region inside which the fluxes in Table 6 have been measured. **c)** Similar to panel **b)** but showing a close-up view of the region around the HMC. The white contours are the ATLASGAL map at 870 μm starting from 20% of the peak emission and increasing by steps of 10%. Superimposed are also the contours of the ^{12}CO (2–1) outflow emission of Fig. 5a starting from a 7σ level (blue and red contours). For each plot, the beam size of the *Herschel* images is shown in the bottom left corner.

Table 6. G023.01−00.41: IR spectral energy distribution within the dashed box of Fig. 10b.

λ (μm)	$F_{\rm int}$ (Jy)	Instrument
3.4	0.013	WISE
3.6	0.025	*Spitzer*/GLIMPSE
4.5	0.19	*Spitzer*/GLIMPSE
4.6	0.28	WISE
5.8	0.38	*Spitzer*/GLIMPSE
8.0	0.19	*Spitzer*/GLIMPSE
12	0.15	WISE
21	4.6	MSX
22	5.2	WISE
24	>7.2	*Spitzer*/MIPSGAL
70	930	*Herschel*/Hi-GAL
160	1090	*Herschel*/Hi-GAL
250	540	*Herschel*/Hi-GAL
350	220	*Herschel*/Hi-GAL
500	92	*Herschel*/Hi-GAL
870	22	APEX/ATLASGAL
1100	5.6	CSO/BGPS

and the following archival data: Wide-field Infrared Survey Explorer (WISE); Galactic Legacy Infrared Mid-Plane Survey Extraordinaire (GLIMPSE; Benjamin et al. 2003); MSX (Egan et al. 2003); MIPSGAL (Carey et al. 2009); APEX Telescope Large Area Survey of the Galaxy (ATLASGAL; Schuller et al. 2009; Csengeri et al. 2014); Bolocam Galactic Plane Survey (BGPS; Drosback et al. 2008). For the *Herschel*/Hi-GAL data, the most recent release was used (obtained in 2011 July with HIPE version 7.0.0), resulting from data reduction with ROMAGAL software (Traficante et al. 2011), where the most relevant image artifacts have been removed by a weighted post-processing of the generalized least square maps (Piazzo et al. 2012). In Fig. 10a and b, we show a *Herschel* picture of the HMSFR G023.01−00.41 obtained with the PACS camera at 160 μm and 70 μm, which indicates that the emission at infrared wavelengths peaks towards the HMC. In Fig. 10c, we also show that the ^{12}CO (2–1) outflow emission discussed in Sect. 3.2.1 is centered on the peak position of the infrared emission and the dusty clump imaged with the APEX telescope at 870 μm. We hence assume the HMC itself to be responsible for most of the far-IR emission from the region and to dominate the bolometric luminosity.

The flux densities were estimated by integrating the emission inside a suitable region chosen to minimize the contamination from nearby cluster members (visible in Fig. 1 of Testi et al. 1998 and Fig. 1 of Furuya et al. 2008). The radius of this region was ∼0.6′ (dashed circle in Fig. 10b) in all cases except the GLIMPSE images, for which a radius of ∼6″ was used, as the angular resolution is significantly higher than in the other images. For the flux calculation, we also subtracted a mean value of the background emission. In each image, the latter was estimated by performing a number of 1D cuts across the peak and measuring the value of the flux at the intersections between such cuts and the border of the selected region over which the integration was performed. Clearly, the background level estimated in this way depends on the direction of the cut, but we find that the corresponding uncertainty on the flux density estimate does not exceed 20%.

We have fitted the SED with the radiative transfer model developed by Robitaille et al. (2007, by using the SED fitting tool[3]), which assumes a pre-main-sequence star with a circumstellar disk, embedded in an infalling flattened envelope with outflow cavities, and allows derivation of a number of physical parameters. While this model cannot take the details of the ongoing star formation toward G023.01−00.41 into account (e.g., Offner et al. 2012), the fit should be good enough to give reliable estimates of *integrated* quantities, such as the luminosity and mass of the clump (solid black profile in Fig. 11). When fixing the distance at 4.6 kpc, the best-fit values are 3.9×10^4 $L_\odot$ and 1.4×10^3 $M_\odot$, respectively, with an interstellar extinction of $A_V = 87$ mag. According to Offner et al. (2012), we caution that the mass value may be significantly overestimated, because

[3] Available at http://caravan.astro.wisc.edu/protostars/

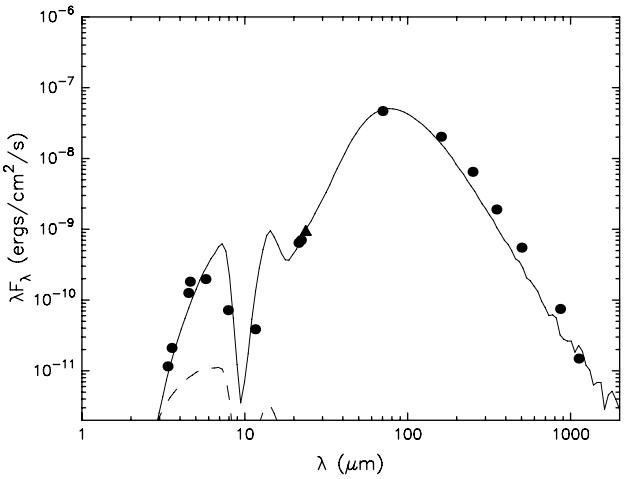

Fig. 11. Spectral energy distribution of G023.01−00.41 from 3.4 μm to 1.1 mm. Dots (triangle) indicate measurements (lower limit) from different telescopes (see Table 6). The SED was fitted with the radiative transfer model developed by Robitaille et al. (2007, and available as a fitting tool at `http://caravan.astro.wisc.edu/protostars/`). The solid black line indicates the best-fitting model.

the model does not take properly the possible presence of a cold component of the clump into account.

4. Discussion

In the following section, we discuss the characteristics of the HMC and associated outflow in G023.01−00.41, in light of two features revealed by our SMA observations on scales from 1″ to 0.″1: 1) the flattened morphology of the core, perpendicular to the outflow direction; and 2) the velocity field revealed through the CH_3CN emission, which appears to outline two mutually orthogonal directions on subarcsecond scales ($\lesssim 3 \times 10^3$ AU). We also recall that the HMC is known to contain a compact source of radio continuum emission and a number of CH_3OH and H_2O maser features (Sanna et al. 2010, their Fig. 4).

4.1. HMC structure

It is interesting to note that the deconvolved size of the core derived from different tracers and with different angular resolutions has a fairly constant ratio of ∼2 between the major and minor axes (Table 3). This result lends support to the existence of a real structure whose characteristics do not depend on the tracer observed. Assuming a circular disk symmetry, this implies that the rotation axis is inclined by 30° with respect to the plane of the sky.

At the largest scale imaged with the compact configuration, the dust emission traces a region as large as 3.″4 (see Table 3), corresponding to a radius of about 8000 AU from the center of the core. The emission from the (3, 3) inversion transition of ammonia arises from a similar region, with a deconvolved angular diameter of 3.″3 (Fig. 1a; see also Codella et al. 1997). The 1.3 mm flux is about ten times the flux recovered at 3 mm by Furuya et al. (2008) within a similar angular extent ($\lesssim$3″), which implies a spectral slope in the mm domain of $\gamma = 3.1 \pm 0.4$ and a dust emissivity exponent $\beta \sim 1$. At the improved resolution of the combined configuration (Compact+VEX), both the dust continuum emission and the bulk emission of the CH_3CN $K = 2$ line present a more compact structure with a major axis of ∼1.″3, corresponding to a radius of ∼3000 AU (Fig. 1c). We also note that the size of the CH_3CN emission inferred from the XCLASS program (∼1.″2; see Table 4) is in good agreement with what is measured from the maps, lending support to the reliability of the fit. Information about the most compact structure that can be imaged with the SMA is obtained from the CH_3OH (15_4–16_3) E transition, whose excitation energy is more than four times higher than for the CH_3CN (12_2–11_2) line. This methanol line unveils a flattened core with a radius of ∼2000 AU (Fig. 1d).

An interesting feature of the emission from the HMC core is that the size of it appears to depend on the tracer: higher excitation lines appear to arise in smaller regions. This trend may be due to increasing gas temperature towards the core center, which in turn would imply the presence of an embedded heating source. However, when comparing different tracers one must take into account that a variation in optical depth may also produce the same effect, with the more opaque lines tracing larger regions. For instance, in Table 3 we show that the deconvolved size of the CH_3CN emission in the $K = 7$ component ($E_{\rm low} \approx 408$ K) is a factor ∼2 less than that of the $K = 2$ and 3 components ($E_{\rm low} \approx 87$ K and 123 K, respectively). But for these lines the opacity increases from the $K = 7$ to the $K = 2$ components (Fig. 2), which might also explain the corresponding increase in size. However, it is possible to demonstrate that for an homogeneous sphere, the ratio between the FWHM of the source in the optically thick and thin limits is $2/\sqrt{3}$, much less than the factor 2 measured by us. We thus conclude that in all likelihood the observed decrease in size is, at least in part, a temperature effect, witnessing the presence of one or more deeply embedded YSOs.

4.1.1. Velocity field of the HMC

As noted in Sect. 3.1.3, the methanol line from the HMC shows a double-peak profile, with blueshifted emission stronger than the redshifted one. In Fig. 1d, we show that such a feature is the result of two partly overlapping components that peak on both sides of the outflow axis. The position of the outflow axis was centered on the dust continuum peak (see Sect. 3.2). Comparison with the spectrum of the CH_3OH maser at 6.7 GHz toward the HMC shows that also the maser lines consist of two groups (Sanna et al. 2010, their Fig. 1), lying at the same red- and blueshifted velocities as the CH_3OH thermal emission. In the VLBI maps, these two groups of maser lines correspond to two distinct clusters of spots coincident with the blue- and redshifted peaks of the thermal emission (blue and red dots in Fig. 1d). Sanna et al. (2010) show that the proper motions of individual masing cloudlets describe two different velocity fields: rotation about an axis with PA ≃ 60° and expansion along the direction of this axis. Assuming centrifugal equilibrium, the dynamical mass estimated from the rotational component of the methanol masers is ∼20 $M_\odot$. The similarity between the spectrum and spatial distribution of the thermal and maser emission suggests that both methanol transitions could be excited in the same physical environment.

The velocity field in the HMC can be further investigated by means of the CH_3CN lines. As outlined in Sect. 3.1, in Fig. 3 one can identify two velocity gradients, one in the direction of the equatorial plane of the flattened HMC with increasing velocities to the SE (PA ≃ −32°) and the other along the perpendicular direction (i.e., in the outflow direction at PA = 58°) with velocities increasing to the SW (Figs. 3c and d). Since there is no evidence of any outflow along the NW–SE direction (Sect. 4.2), a possible interpretation of this velocity field is that the CH_3CN gas is tracing *both* expansion along the outflow

direction *and* rotation perpendicular to it (see also Fig. 1b). As explained in Sect. 3.1.2, the CH_3CN velocity gradient along the outflow direction (see Fig. 3c) is reproduced well by a linear fit (corr. coeff. 0.8) and agrees with the velocity gradient detected in the SiO (5–4) emission (Fig. 7b) and the one outlined by the methanol masers in the $p - v$ plot of Fig. 3c (red triangles; Sanna et al. 2010). These results suggest that, even inside a radius of ∼0.″25 from the center of the HMC, the CH_3CN emission is affected by the outflow expansion. A similar velocity gradient is also seen along the direction perpendicular to the outflow (Fig. 3d). The presence of two, orthogonal velocity gradients with similar slopes explains why the CH_3CN (6–5) maps by Furuya et al. (2008, their Fig. 11) did not reveal a clear velocity gradient, since their observations had a three times less resolution than ours.

Beyond the FWHM of the CH_3CN lines (red and blue dashed lines in Fig. 3d), the emission along a PA = −32° appears to peak at zero offset, namely close to the outflow axis. This behavior may indicate that the high velocity emission is dominated by gas entrained in the outflow, but it is also expected if the gas is undergoing Keplerian rotation. To describe this scenario, we plot in Fig. 3d the velocity pattern corresponding to Keplerian rotation about a 19 $M_\odot$ star, where the inclination of the disk with respect to the line-of-sight (30°; see Sect. 4.1) has been taken into account. While the Keplerian profile appears consistent with our data points, it is not sufficient to claim the existence of a Keplerian disk. However, the presence of a velocity gradient inside the line FWHM seems clear (Fig. 3b), and it is very reasonable that such a gradient could be due to rotation (albeit not necessarily Keplerian) about an equilibrium mass on the order of 19 $M_\odot$, in agreement with what is estimated with the CH_3OH maser spots (see above). In Fig. 3d, we show indeed that the maser points lying within a distance of 0.25 arcsec from the dust continuum peak (red triangles) agree well with the peak distribution of the CH_3CN emission.

With this in mind, in the following we adopt the working hypothesis that the HMC contains a flattened structure whose rotation, about an axis close to 58° on the plane of the sky, implies an equilibrium mass of ∼19 $M_\odot$.

One may wonder what fraction of this mass is contributed by the gas lying inside 0.″25 (or 1150 AU). The gas mass can be estimated from the dust continuum emission (e.g., Hildebrand 1983), assuming thermal equilibrium between gas and dust at a temperature of 195 K, derived from the CH_3CN lines (see Table 4). Our calculation uses a dust absorption coefficient of 0.8 $cm^2\ g^{-1}$ at the observing frequency and a standard gas-to-dust mass ratio of 100 (Ossenkopf & Henning 1994). Inside a radius of 0.″65 or 3000 AU, corresponding to the region where both the CH_3CN lines and the dust emission are detected with the combined array, we estimate a mass of 8.5 ± 0.8 $M_\odot$ and a mean column density of $(4.9 \pm 0.4) \times 10^{23}\ cm^{-2}$. The quoted errors correspond to the 5σ uncertainty of the flux measurement, although we stress that the main source of uncertainty comes from the poorly known dust properties. Even assuming a density profile as steep as $n \propto R^{-2}$, the gas mass inside 1150 AU cannot be greater than 3.3 $M_\odot$. We conclude that the stellar component must dominate the ∼19 $M_\odot$ estimated above.

4.1.2. Stability of the rotating HMC

It is also worth computing the mass in the envelope beyond the 3000 AU radius. For this purpose, we consider the difference between the continuum flux measured with the compact SMA configuration and the one measured with the combined configuration, and assume a gas and dust temperature equal to that obtained by Codella et al. (1997) from the NH_3 lines (58 K). This choice is justified by the fact that ammonia observations were sensitive to more extended structures than those imaged in our CH_3CN maps, similar to the largest scale imaged with the SMA for the dust emission (see Sect. 4.1). We thus estimate a mass of 12 ± 4 $M_\odot$ for the outer regions of the envelope, comparable to the one enclosed inside 3000 AU and to the putative stellar mass. An envelope whose mass is close to the one of the central star(s) is expected to develop instabilities (see, e.g., Cesaroni et al. 2007, and references therein).

It is useful of interest to verify whether or not the flattened, rotating structure observed in G023.01−00.41 is stable with respect to axisymmetric gravitational disturbances, assuming that we can approximate the system as a thin disk. Following the simplified approach outlined in Cesaroni et al. (2007), we estimate the stability parameter Q (Toomre 1964) at the maximum radius of emission for both the inner (inside 3000 AU) and outer (between 3000 and 8000 AU) regions of the HMC. The Q parameter is proportional to the product of the sound speed and the angular velocity at a given radius and inversely proportional to the disk surface density at the same radius. The condition of instability is $Q < 1$, which implies that a disk tends to form massive condensations. At the inner radius of 3000 AU, we estimate $Q \simeq 9$, by replacing the sound speed with the linewidth of the CH_3CN lines ($FWHM/\sqrt{8 \ln 2}$). At the outer radius of 8000 AU, using the NH_3 linewidth (from Table 8 of Codella et al. 1997) and the mean surface density computed from the mass of 12 $M_\odot$, we obtain a lower value, $Q \simeq 3.5$. This estimate has to be taken as an upper limit because the NH_3 linewidth was measured at the peak position of the VLA map. At both radii the main support to gravitational instabilities is provided by turbulence, which dominates the linewidth, since thermal broadening accounts for less than 1 km s^{-1}. While the error on these values of Q is certainly large, the result that Q decreases with distance from the HMC center appears more robust, because most sources of uncertainties affect both estimates of Q equally. We thus conclude that the observed rotating structure appears to be progressively more unstable at larger radii.

4.2. Outflow morphology and dynamics

In Fig. 5a, we show that the ^{12}CO emission extends along the NE–SW direction up to a distance of ∼0.5 pc from the center of the HMC, with the redshifted emission located to the SW. The ^{12}CO outflow mass computed from the J = 2–1 transition is a factor ∼8 less than estimated by Furuya et al. (2008) from the J = 1–0 transition (after correcting for the new distance adopted by us). We believe that this discrepancy is compatible with the large uncertainties of the ^{12}CO (1–0) measurements (see Table 7 of Furuya et al. 2008), and may also be affected by contamination from extended emission in the ^{12}CO (1–0) maps. For this reason, we rely upon our estimates in the following discussion.

In a region four times smaller than that traced by ^{12}CO and ^{13}CO, the SiO (5–4) line emission traces a bipolar outflow in the same direction as the ^{12}CO (2–1) emission, with the blue- and redshifted lobes located to the NE and SW, respectively (Fig. 5d). We stress that the direction of the outflow (PA = 58°) coincides with the rotation axis of the flattened HMC (Fig. 1). It is also worth noting that the outflow direction agrees with both the orientation and proper motion of the H_2O maser jet detected by Sanna et al. (2010, their Fig. 5b). The maser emission arises

within 2000 AU from the dust continuum peak detected with the SMA. This evidence supports the existence of a powering source at the center of the dusty core that dominates the outflow dynamics on all scales.

The CO outflow lobes appear very collimated with a width-to-length ratio ∼0.3, which suggests that the outflow axis lies close to the plane of the sky, in agreement with the small inclination (30°) of the disk-like structure of the HMC with respect to the line-of-sight (see Sect. 4.1). This is also consistent with the detection of some faint blueshifted emission from the red lobe, and vice versa, as expected when the lobes are partly crossing the plane of the sky. In Table 5, we also report the parameters of the outflow corrected for an inclination angle of 30°.

Unlike the $C^{18}O$ (1–0) line, the $C^{18}O$ (2–1) line emission peaks at the position of the HMC with a fainter tail extending to the SE (Fig. 5c), towards the peak of the J= 1–0 line (see Fig. 6c of Furuya et al. 2008). The overall bulk emission of the $C^{18}O$ gas to the NE presents a curved morphology, outlined by the dashed pattern in Fig. 5c. While the faint, high-velocity $C^{18}O$ emission is aligned with the outflow axis, the quiescent $C^{18}O$ gas (within the FWHM of the CH_3CN emission) might arise from the outer edges of the blueshifted outflow lobe.

The channel maps reveal a clumpy structure along the outflow axis (Fig. 8), possibly related to different ejection episodes. Such clumpyness is also visible in the $p-v$ plot in Fig. 7, where one may also appreciate the lack of emission close to the systemic velocity, likely owing to extended structures filtered out by the interferometer. In contrast, the SiO emission in Fig. 7 is detected at all velocities, although the peak appears offset with respect to the systemic velocity. This agrees with the idea that the SiO emission originates mostly in the high-velocity gas in the post-shock region, where the SiO molecules are believed to form (see Sect. 3.2.2).

A remarkable fact is that the blueshifted emission in all CO isotopomers is significantly fainter and much patchier than the redshifted emission. This is clearly seen in the channel maps, as well as in the mean spectra in Fig. 6, which reveal multiple velocity components below 80 km s^{-1}, most likely due to unrelated molecular clouds along the line of sight to G023.01−00.41. In contrast, the redshifted emission is much more coherent and the corresponding spectral profile smoother. As expected, the contamination by spurious components at blueshifted velocities becomes much less pronounced in the optically thinner $C^{18}O$ line and is basically absent in the SiO transition. We conclude that most of the features observed in the blueshifted channels are due to molecular gas along the line of sight, which has no relationship with the region of interest for us. This explains the presence of prominent blueshifted emission on the same side as the red lobe, especially the elongated ^{13}CO structure centered at (−10″, −15″) and spanning a velocity range from 64 to 66.2 km s^{-1} (see Fig. 9). The same structure, named clump B in Sect. 3.2.1, looks fainter and more fragmented in the corresponding ^{12}CO maps (Fig. 8), which confirms that the emission originates in an extended cloud along the line of sight, partly resolved out in the optically thicker transition.

In the calculation of the outflow parameters we have been careful to select only the emission most likely associated with the outflow, both in space and velocity. We are thus confident that the parameters listed in Table 5 are reliable in this respect. Despite the large uncertainty on the SiO abundance, which in turn affects the reliability of the corresponding outflow parameters, we note that the latter differ only by a factor ∼4 from those obtained from the CO line. All these facts make us confident that our estimates are reliable.

Finally, we note that a momentum rate of 6×10^{-3} $M_\odot$ km s^{-1} yr^{-1}, determined from the ^{12}CO (2–1) emission after correcting for the inclination angle of the outflow, is in good agreement with the bolometric luminosity, according to a well known empirical relation (see Fig. 4 of Beuther et al. 2002). This result lends further support to our estimate of the luminosity (and mass) of the embedded star.

4.3. Nature of the embedded source(s) in the HMC

In Sect. 4.1 we have proposed a scenario where the HMC is rotating down to scales on the order of 1000 AU, and the corresponding equilibrium mass is ≲19 $M_\odot$. We have also shown that most of this mass must be in the form of (proto)stars. In the following, we want to set constraints on the nature of these objects using the information obtained from the IR and free-free radio emission.

In Sect. 3.3, we concluded that in all likelihood the HMC is dominating the IR flux of the region (see Fig. 10) so is responsible for the bolometric luminosity of 3.9×10^4 $L_\odot$. This conclusion is strengthened by a simple calculation of the HMC luminosity if it was in thermal equilibrium at the temperature of the CH_3CN gas. By using $T_{\rm rot}$ = 195 K and assuming LTE inside the HMC, within the radius of CH_3CN emission (≲3000 AU) the Stefan-Boltzmann law ($L \propto T^4$) yields a bolometric luminosity of $\sim 5 \times 10^4$ $L_\odot$, which is in remarkable agreement with the luminosity obtained from the measured SED. For a ZAMS star, the measured luminosity is comparable to the expected luminosity ($\sim 5 \times 10^4$ $L_\odot$) of a 19 $M_\odot$ star (e.g., Eq. (13) of Hosokawa et al. 2010), suggesting that a single object with a O9.5 spectral type could justify the observed luminosity. However, as noted by Sanna et al. (2010), such a star should produce much more Lyman continuum photons than those estimated from the measured radio continuum ($\sim 3 \times 10^{45}$ s^{-1}). In fact, the free-free emission, which peaks at the center of the HMC (Sanna et al. 2010, their Table 1 and Fig. 4), corresponds to photo ionization by a ZAMS star with a B1 spectral type, namely a ZAMS luminosity that is an order of magnitude less than the observed luminosity (e.g., Schaller et al. 1992). How may one reconcile this evidence with the measured bolometric luminosity?

A first possibility is that ongoing accretion onto the star is quenching the formation of an H II region (e.g., Keto 2002), allowing only a small fraction of the Lyman continuum photons to escape through the outflow. The measured free-free continuum would thus lead to an underestimate of the true Lyman photons, hence of the stellar luminosity. Alternatively, the free-free emission could be tracing a thermal jet where the ionization is due to shocks in the ejected material, as we have speculated in Sanna et al. (2010) on the basis of the radio continuum morphology and spectral index between 3.6 and 1.3 cm. As a matter of fact, jets like these – albeit rare – have been found to be associated with high-mass stars (e.g., Anglada 1996).

Another explanation may be that we are dealing with a massive, bloated pre-ZAMS star as those modeled by Hosokawa et al. (2010) in the presence of high accretion rates (≳10^{-3} $M_\odot$ yr^{-1}). Objects of this type are much colder than a ZAMS star with the same luminosity and are hence very weak Lyman continuum emitters. However, the accretion rate onto the star should be a few times less than the mass loss rate determined from the outflow tracers (e.g., Behrend & Maeder 2001), which in our case implies a value ≲10^{-4} $M_\odot$ yr^{-1} (see Table 5). Also, objects as massive as 19 $M_\odot$ are not expected to have a pre-ZAMS phase (see Fig. 14 of Hosokawa et al. 2010). Therefore, we consider this scenario quite unlikely.

Finally, one should consider the possibility that the total mass (19 $M_\odot$) is contributed by multiple lower mass stars, rather than a single O9.5 star. This hypothesis cannot be proved or ruled out by direct observations, as the angular resolution of the available images is insufficient to resolve a tight binary or a multiple system in the HMC. Splitting a mass of 19 $M_\odot$ into smaller stars would reduce the Lyman continuum output significantly and make it consistent with that estimated from the radio continuum. However, the bolometric luminosity would also decrease well below the observed value ($L_{\star,\mathrm{ZAMS}} \propto M_\star^2$), which appears inconsistent with the fact that most of the observed emission in the infrared originates in the HMC (see Sect. 3.3).

In conclusion, we believe that, with the current data, the most reliable scenario for G023.01−00.41 is that of a deeply embedded massive ($\lesssim$19 $M_\odot$) ZAMS star, still undergoing accretion from the parental core, possibly surrounded by an accretion disk, and powering a radio jet and a pc-scale outflow.

5. Summary and conclusions

We used the SMA to image various hot-core and outflow tracers from the high-mass star-forming region G023.01−00.41 at 1.3 mm. We have also combined the *Herschel*/Hi-GAL data with ancillary archival data to reconstruct the SED associated with the HMC in G023.01−00.41 (between 3.4 μm and 1.1 mm) and derive its luminosity. In this paper, we focused on a comparison of the gas dynamics in the inner HMC, on scales $\lesssim$0.01 pc, with respect to what is inferred from typical outflow tracers, on scales $\gtrsim$0.1 pc. Our main results can be summarized as follows.

1. We find that the HMC core is significantly flattened (width-to-length ratio ∼2), which corresponds to an inclination of 30° under the assumption that we are observing an oblate core tilted with respect to the line of sight. Also, the size of the core appears to decrease with excitation energy of the observed transition, suggesting the presence of a temperature gradient due to embedded YSOs. From the mean CH_3CN spectrum within a radius of ∼3000 AU from the HMC center, we infer a rotational temperature of ∼195 K.
2. The CH_3CN emission appears to trace two distinct velocity fields, one consistent with expansion along the outflow axis, the other suggesting rotation about the same axis (possibly Keplerian), in good agreement with the (3D) velocity field traced by methanol masers. The central mass implied by the rotational component is ∼19 $M_\odot$, after taking an inclination of the rotation axis of 30° into account. This value is consistent with the bolometric luminosity of the G023.01−00.41 region (∼4×10^4 $L_\odot$) estimated by fitting the SED.
3. We estimated the Tommre Q stability parameter at two different radii in the putative disk, and find that Q decreases significantly from small to large radii, consistent with the disk being more stable close to the central star(s), as expected.
4. The outflow emission imaged in the CO isotopomers and SiO(5–4) line matches the direction of the rotation axis (PA = 58°) of the flattened HMC well. The outflow is well collimated with a width-to-length ratio for each lobe of about 0.3. The energetics of the molecular outflow, such as its momentum rate of 6×10^{-3} $M_\odot$ km s^{-1} yr^{-1}, is in good agreement with the energetics expected for the measured bolometric luminosity.

We conclude that the HMC in G023.01−00.41 is most likely hosting an O9.5 (proto)star lying at its center, powering the bipolar outflow observed on the parsec scale, and it shows clear proof of rotation up to a radius of ∼1000 AU. Higher angular resolution observations are needed in order to confirm that the HMC is indeed hosting a single massive star, to trace the inner rotation curve, and to find out whether accretion is still going on inside the HMC.

Acknowledgements. Comments from the anonymous referee, which helped improving our paper, are gratefully acknowledged. Financial support by the European Research Council for the ERC Advanced Grant GLOSTAR (ERC-2009-AdG, Grant Agreement no. 247078) is gratefully acknowledged. This research made use of the myXCLASS program (https://www.astro.uni-koeln.de/projects/schilke/XCLASS), which accesses the CDMS (http://www.cdms.de) and JPL (http://spec.jpl.nasa.gov) molecular databases. This publication makes use of data products from the Wide-field Infrared Survey Explorer, which is a joint project of the University of California, Los Angeles, and the Jet Propulsion Laboratory/California Institute of Technology, funded by the National Aeronautics and Space Administration.

References

Anglada, G. 1996, in Radio Emission from the Stars and the Sun, eds. A. R. Taylor, & J. M. Paredes, ASP Conf. Ser., 93, 3
Behrend, R., & Maeder, A. 2001, A&A, 373, 190
Benjamin, R. A., Churchwell, E., Babler, B. L., et al. 2003, PASP, 115, 953
Beuther, H., Schilke, P., Sridharan, T. K., et al. 2002, A&A, 383, 892
Brunthaler, A., Reid, M. J., Menten, K. M., et al. 2009, ApJ, 693, 424
Cabrit, S., & Bertout, C. 1990, ApJ, 348, 530
Carey, S. J., Noriega-Crespo, A., Mizuno, D. R., et al. 2009, PASP, 121, 76
Cesaroni, R., Galli, D., Lodato, G., Walmsley, C. M., & Zhang, Q. 2007, in Protostars and Planets V, eds. B. Reipurth, D. Jewitt, & K. Keil (University of Arizona Press), 197
Codella, C., Testi, L., & Cesaroni, R. 1997, A&A, 325, 282
Comito, C., Schilke, P., Phillips, T. G., et al. 2005, ApJS, 156, 127
Csengeri, T., Urquhart, J. S., Schuller, F., et al. 2014, A&A, in press, DOI:10.1051/0004-6361/201322434
Cyganowski, C. J., Brogan, C. L., Hunter, T. R., & Churchwell, E. 2009, ApJ, 702, 1615
Drosback, M. M., Aguirre, J., Bally, J., et al. 2008, in AAS Meeting Abstracts #212, BAAS, 40, 271
Egan, M. P., Price, S. D., & Kraemer, K. E. 2003, in AAS Meeting Abstracts, BAAS, 35, 1301
Furuya, R. S., Cesaroni, R., Takahashi, S., et al. 2008, ApJ, 673, 363
Gibb, A. G., Richer, J. S., Chandler, C. J., & Davis, C. J. 2004, ApJ, 603, 198
Gibb, A. G., Davis, C. J., & Moore, T. J. T. 2007, MNRAS, 382, 1213
Hildebrand, R. H. 1983, QJRAS, 24, 267
Hosokawa, T., Yorke, H. W., & Omukai, K. 2010, ApJ, 721, 478
Keto, E. 2002, ApJ, 580, 980
Kuiper, R., & Yorke, H. W. 2013, ApJ, 763, 104
Molinari, S., Swinyard, B., Bally, J., et al. 2010, PASP, 122, 314
Müller, H. S. P., Schlöder, F., Stutzki, J., & Winnewisser, G. 2005, J. Mol. Struct., 742, 215
Offner, S. S. R., Robitaille, T. P., Hansen, C. E., McKee, C. F., & Klein, R. I. 2012, ApJ, 753, 98
Ossenkopf, V., & Henning, T. 1994, A&A, 291, 943
Piazzo, L., Ikhenaode, D., Natoli, P., et al. 2012, IEEE Transactions on Image Processing, 21, 3687
Qiu, K., Zhang, Q., Wu, J., & Chen, H.-R. 2009, ApJ, 696, 66
Robitaille, T. P., Whitney, B. A., Indebetouw, R., & Wood, K. 2007, ApJS, 169, 328
Sanna, A., Moscadelli, L., Cesaroni, R., et al. 2010, A&A, 517, A78
Sanna, A., Moscadelli, L., Cesaroni, R., & Goddi, C. 2012, in IAU Symp. 287, eds. R. S. Booth, W. H. T. Vlemmings, & E. M. L. Humphreys, 396
Schaller, G., Schaerer, D., Meynet, G., & Maeder, A. 1992, A&AS, 96, 269
Schuller, F., Menten, K. M., Contreras, Y., et al. 2009, A&A, 504, 415
Testi, L., Felli, M., Persi, P., & Roth, M. 1998, A&AS, 129, 495
Toomre, A. 1964, ApJ, 139, 1217
Traficante, A., Calzoletti, L., Veneziani, M., et al. 2011, MNRAS, 416, 2932
Wilson, T. L., & Rood, R. 1994, ARA&A, 32, 191
Zinnecker, H., & Yorke, H. W. 2007, ARA&A, 45, 481